Seamless 5G Automotive Connectivity with Integrated Satellite Terrestrial Networks in C-Band

Hung Nguyen-Kha†, Vu Nguyen Ha†, Eva Lagunas†, Symeon Chatzinotas†, and Joel Grotz‡
†*Interdisciplinary Centre for Security, Reliability and Trust (SnT), University of Luxembourg, Luxembourg*
‡*SES S.A., Luxembourg*

***Abstract*—This paper examines integrated satellite-terrestrial networks (ISTNs) in urban environments, where terrestrial networks (TNs) and non-terrestrial networks (NTNs) share the same frequency band in the C-band which is considered the promising band for both systems. The dynamic issues in ISTNs, arising from the movement of low Earth orbit satellites (LEOSats) and the mobility of users (UEs), are addressed. The goal is to maximize the sum rate by optimizing link selection for UEs over time. To tackle this challenge, an efficient iterative algorithm is developed. Simulations using a realistic 3D map provide valuable insights into the impact of urban environments on ISTNs and also demonstrates the effectiveness of the proposed algorithm.**

I. Introduction

Recently, ISTNs have emerged as a promising solution for achieving seamless connectivity and meeting high data rate demands [1]–[7]. Particularly, as the connection number and the service demand increase rapidly, especially in urban areas, TNs struggle to ensure a high data rate for massive connectivity. Additionally, ensuring TN coverage in urban areas requires dense BS deployment which is a difficult task. In contrast, satellite networks offer ubiquitous, seamless connectivity, coverage enhancement, and data offloading. Therefore, ISTNs leverage the strengths of both systems, ensuring high-quality, seamless connections across various environments [1]–[3]. Additionally, due to the rapid increase in data demand and the proliferation of devices, 3GPP has highlighted the potential of ISTNs to operate TN and NTN systems in the same band, such as the C-band [8]. Due to long propagation and broadband properties, the C-band has been widely used for satellite services. Recently, these qualities made it highly attractive in 5G for good coverage and high data throughput, facilitated by the US FCC and RSPG in Europe [9], [10], and standardized by 3GPP for 5G NR. The convergence of ISTN development and the global interest in the C-band envisions many benefits for future ISTNs. However, operating in the same band introduces critical cross-network interference issues in various environments. Urban environments, in particular, present complex characteristics that significantly impact the channel gain between satellites and ground segments [11]. Additionally, the movement of UEs and LEOSats introduces dynamics and time-varying changes [12]–[15]; hence, environmental characteristics and movements should be considered for ISTN designs.

The spectral coexistence of TN and satellite networks has been studied extensively [8], [16]–[19]. The authors in [16] investigated coexistence systems at the millimeter-wave frequency, analyzing co-channel and adjacent channel interference in NTNs. In [17], the authors analyzed the interference and out-of-band emission caused by 5G networks on fix-satellite-service (FSS) earth stations in C-band coexistence scenarios. The study in [18] examined scenarios where TNs and NTNs operate in adjacent 5G NR bands in the S-band, analyzing the impact of adjacent channel interference on system performance. In [19], the authors explored coexistence scenarios in the S-band, analyzing co-channel interference, network coverage, and achievable rates in different cases. Notably, the 3GPP recently discussed various coexistence scenarios between satellite and TNs in [8], analyzing throughput loss in S-band. However, these analyses rely on statistical channels without capturing the geographical characteristics of complex environments.

Therefore, novel solutions considering urban-environment characteristics and terminal mobility to address critical cross-network interference are essential. This paper studies the ISTNs in an urban area operating in the C-band. Considering the mobility of UEs and LEOSats, we formulate a sum-rate (SR) maximization problem to optimize link selection for UEs, under the BS and LEOSat load constraints. This problem is challenging to solve directly due to the non-convex rate function. To address this efficiently, we employ the successive-convex-approximation (SCA) approach [20]–[23] to develop an iterative algorithm. In the simulation, the ray-tracing method and an actual 3D map are utilized to capture urban characteristics. Additionally, the routes of the UEs are obtained using Google Navigator. The simulated heatmap of the link budget provides valuable insights into the effects of urban characteristics on ISTNs. For the max-SR problem, the numerical results demonstrate the efficiency of the proposed algorithm in terms of SR, compared to a proposed greedy-based algorithm.

II. System Model

This work studies the downlink ISTN systems in the urban environments as depicted in Fig. 1, wherein LEOSats and TNs operate in the same frequency band, i.e., C-band, during a time-windows of N_{TS} TSs. The system includes M LEOSats, N BSs, and K UEs (cars). We further assume that the UEs can be served by the LEOSat, one BS, or both at any time.

A. Tx-UE Channel Model

Let $h_{n,k}^t$ and $g_{m,k}^t$ be the channel gain of $\mathsf{BS}_n - \mathsf{UE}_k$ and $\mathsf{LEOSat}_m - \mathsf{UE}_k$ links at TS t, respectively. The channel gain is calculated by the inverse of path-loss (PL). By utilizing the multi-path channel model, the equivalent PL of Tx-UE (Tx is LEOSat/BS) link can be modeled as

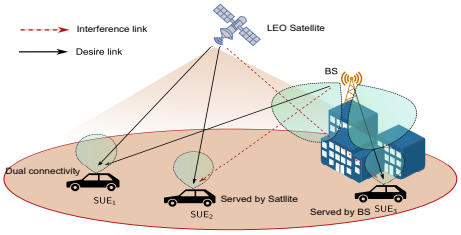

Fig. 1: System model of ISTNs.

$$L_{\mathsf{UE}}^{\mathsf{Tx}}[\text{dB}] = -\log_{10}\left(\left|\sum_{i=0}^{N_{\text{ray}}} \frac{G_{\mathsf{r}}(\theta_i^{\mathsf{a}},\varphi_i^{\mathsf{a}})G_{\mathsf{t}}(\theta_i^{\mathsf{d}},\varphi_i^{\mathsf{d}})}{L_i L_{\mathsf{B}}} e^{-j\phi_i}\right|^{-1}\right), \quad (1)$$

wherein N_{ray} is the number of propagation rays from the Tx to the UE. L_i and ϕ_i are the propagation loss and phase delay of ray i. $G_{\mathsf{r}}(\cdot)$ and $G_{\mathsf{t}}(\cdot)$ are the antenna gain patterns of the UE and the Tx. $(\theta_i^{\mathsf{a}},\varphi_i^{\mathsf{a}})$ the elevation and azimuth angles of arrive at the UE, and $(\theta_i^{\mathsf{d}},\varphi_i^{\mathsf{d}})$ are angles of departure at the Tx corresponding to ray i. Especially, ray i, $i \geq 1$, is the LoS ray or the ray reaching the UE by reflection or diffraction on the obstacles in the environment. Ray $i = 0$ is the ray propagating through the wall to reach the UE, the loss component L_0 of this ray can be modeled $L_0 = L_{\mathsf{FS}} + 2L_{\mathsf{wall}}$, wherein L_{FS} is the free space path loss and L_{wall} is the penetration loss which is given in [24]. In addition, L_{B} is the other basic loss defined by [24] and [25] for TN and NTN links, respectively.

Subsequently, the antenna gain pattern of LEOSats, BSs, and UEs are modeled as follows. Regarding the LEOSats, we employ the antenna gain pattern modeled by the Bessel function for that satellite given in [25]. The BS's antenna gain is modeled by the non-active antenna system pattern expressed in [8]. Additionally, the UE (the car) is assumed to be equipped with a patch antenna array on the rooftop, wherein its antenna pattern can be obtained by the MATLAB antenna toolbox.

B. User Association Model

Regarding the BS-UE link, we introduce a binary variable $\boldsymbol{\alpha} \triangleq [\alpha_{n,k}^t]_{\forall(n,k,t)}$ to indicate the BS-UE association: $\alpha_{n,k}^t = 1$ if UE_k connects to BS_n at TS t and $\alpha_{n,k}^t = 0$ otherwise. In addition, one assumes that each UE can connect to at most one BS at each TS, which is ensured by the constraint:

$$(C1): \quad \sum_{\forall n} \alpha_{n,k}^t \leq 1, \forall(k,t). \quad (2)$$

Additionally, one assumes that BS_n can serve at most ψ_n^{B} users. Let $\eta_n^{\mathsf{B},t}$ be the number of other connected users of BS_n at TS t, the number of connections at each BS can be ensured as

$$(C2): \quad \sum_{\forall k} \alpha_{n,k}^t \leq \psi_n^{\mathsf{B}} - \eta_n^{\mathsf{B},t}, \forall(n,t), \quad (3)$$

Subsequently, regarding the LEOSat-UE association, we introduce another binary variable $\boldsymbol{\beta} \triangleq [\beta_{m,k}^t]_{\forall(m,k,t)}$ such that $\beta_{m,k}^t = 1$ if UE_k connects to LEOSat_m at TS t and $\beta_{m,k}^t = 0$ otherwise. In addition, we assume that each UE can connect to at most one LEOSat at each TS, which is ensured as

$$(C3): \quad \sum_{\forall m} \beta_{m,k}^t \leq 1, \forall(k,t). \quad (4)$$

Assuming that LEOSat_m can serve at most ψ_m^{S} users at each TS, let $\eta_m^{\mathsf{S},t}$ be the number of other connected users to LEOSat_m at TS t, the UE connection number at each LEOSat obeys

$$(C4): \quad \sum_{\forall k} \beta_{m,k}^t \leq \psi_m^{\mathsf{S}} - \eta_m^{\mathsf{S},t}, \forall(m,t). \quad (5)$$

Furthermore, we assume that dual connectivity is supported, i.e., UE can connect to both BS and LEOSat simultaneously. To ensure seamless connectivity, one assumes that each UE has at least one connectivity at each TS, guaranteed by

$$(C5): \quad \sum_{\forall n} \alpha_{n,k}^t + \sum_{\forall m} \beta_{m,k}^t \geq 1, \forall(k,t). \quad (6)$$

C. Transmission Model

We assume that components within the same networks are coordinated for interference mitigation. Hence, one assumes that the intra-network interference is negligible and only cross interference between TNs and NTNs is considered. Consequently, if UE_k connects to BS_n, its SINR can be given as

$$\gamma_{n,k}^{\mathsf{B},t}(\boldsymbol{\alpha},\boldsymbol{\beta}) = \frac{\alpha_{n,k}^t P_n^{\mathsf{B}} h_{n,k}^t}{\sum_{\forall m}(\eta_m^{\mathsf{S},\mathsf{t}} + \sum_{\forall k'} \beta_{m,k'}^t) P_m^{\mathsf{S}} g_{m,k}^t + \sigma_k^2}, \quad (7)$$

wherein σ_k^2 is the AWGN power at UE_k. P_n^{B} and P_m^{S} are the transmit power of BS_n and LEOSat_m for each of their connected users, respectively. These transmit powers are uniformly allocated as $P_n^{\mathsf{B}} = P_n^{\mathsf{B},\max}/\psi_n^{\mathsf{B}}$ and $P_m^{\mathsf{S}} = P_m^{\mathsf{S},\max}/\psi_m^{\mathsf{S}}$. The throughput from BS_n to UE_k at TS t can be computed as

$$R_{n,k}^{\mathsf{B},t}(\boldsymbol{\alpha},\boldsymbol{\beta}) = \log(1 + \gamma_{n,k}^{\mathsf{B},t}(\boldsymbol{\alpha},\boldsymbol{\beta})). \quad (8)$$

Regarding the LEOSat-UE connection, if UE_k connects to LEOSat_m, the corresponding SINR can be expressed as

$$\gamma_{m,k}^{\mathsf{S},t}(\boldsymbol{\alpha},\boldsymbol{\beta}) = \frac{\beta_{m,k}^t P_m^{\mathsf{S}} g_{m,k}^t}{\sum_{\forall n}(\eta_n^{\mathsf{B},\mathsf{t}} + \sum_{\forall k'} \alpha_{n,k'}^t) P_n^{\mathsf{B}} h_{n,k}^t + \sigma_k^2}. \quad (9)$$

The throughput of $\mathsf{LEOSat}_m - \mathsf{UE}_k$ link at TS t is given as

$$R_{m,k}^{\mathsf{S},t}(\boldsymbol{\alpha},\boldsymbol{\beta}) = \log(1 + \gamma_{m,k}^{\mathsf{S},t}(\boldsymbol{\alpha},\boldsymbol{\beta})). \quad (10)$$

Hence, the throughput of UE_k at TS t can be expressed as

$$R_k^t(\boldsymbol{\alpha},\boldsymbol{\beta}) = \sum_n R_{n,k}^{\mathsf{B},t}(\boldsymbol{\alpha},\boldsymbol{\beta}) + \sum_m R_{m,k}^{\mathsf{S},t}(\boldsymbol{\alpha},\boldsymbol{\beta}). \quad (11)$$

D. Problem Formulation

The UEs mobility, LEOSats movement, and complexity of urban areas lead to the time-varying change in the system. Therefore, the UEs need to change the connections between BSs/LEOSats over time to maximize their SR. The max-SR problem can be mathematically formulated as

$$\max_{\boldsymbol{\alpha},\boldsymbol{\beta}} \quad \sum_{k,t} R_k^t(\boldsymbol{\alpha},\boldsymbol{\beta}) \quad \text{s.t. } (C1) - (C5). \quad (12)$$

It can be seen that problem (12) is non-convex due to the non-convexity of the rate formulas in the objective.

III. Proposed Sum-Rate Maximization Solution

Problem (12) is difficult to solve directly due to the binary variable $\boldsymbol{\alpha}$ and $\boldsymbol{\beta}$, and the non-convexity of the objective function. Hence, we first relax the binary variables into the continuous ones as $\alpha_{n,k}^t \in [0,1], \forall(n,k,t)$ and $\beta_{m,k}^t \in [0,1], \forall(m,k,t)$, respectively. Besides, to convexify the rate functions in the objective function, let us perform the rate functions by their lower bounds $\lambda_{n,k}^{\mathsf{B},\mathsf{t}}$ and $\lambda_{m,k}^{\mathsf{S},\mathsf{t}}$ as

$$\lambda_{n,k}^{\mathsf{B},\mathsf{t}} \leq R_{n,k}^{\mathsf{B},t}(\boldsymbol{\alpha},\boldsymbol{\beta}), \quad \forall n,k,t, \quad (13a)$$

$$\lambda_{m,k}^{\mathsf{S},\mathsf{t}} \leq R_{m,k}^{\mathsf{S},t}(\boldsymbol{\alpha},\boldsymbol{\beta}), \quad \forall m,k,t. \quad (13b)$$

Algorithm 1 PROPOSED ITERATIVE ALGORITHM

1: Set $i = 0$ and generate an initial point $(\boldsymbol{\mu}^{\mathsf{B},(0)}, \boldsymbol{\mu}^{\mathsf{S},(0)})$.
2: **repeat**
3: Solve (17) to obtain $(\boldsymbol{\alpha}^\star, \boldsymbol{\beta}^\star, \boldsymbol{\lambda}^{\mathsf{B},\star}, \boldsymbol{\lambda}^{\mathsf{S},\star}, \boldsymbol{\mu}^{\mathsf{B},\star}, \boldsymbol{\mu}^{\mathsf{S},\star})$.
4: Update $(\boldsymbol{\mu}^{\mathsf{B},(i)}, \boldsymbol{\mu}^{\mathsf{S},(i)}) := (\boldsymbol{\mu}^{\mathsf{B},\star}, \boldsymbol{\mu}^{\mathsf{S},\star})$ and set $i = i + 1$.
5: **until** Convergence
6: Recovery variables $\boldsymbol{\alpha}$ and $\boldsymbol{\beta}$ by (18).
7: **Output:** The solution $(\boldsymbol{\alpha}^\star, \boldsymbol{\beta}^\star)$.

However, constraint (13) is still non-convex. Subsequently, (13) can be convexified by the following proposition.

Proposition 1: *Constraints in* (13) *can be convexified as*

$$\log(\alpha^t_{n,k}P^{\mathsf{B}}_n h^t_{n,k}+\sum_{\forall m}(\eta^{\mathsf{S,t}}_m+\sum_{\forall k'}\beta^t_{m,k'})P^{\mathsf{S}}_m g^t_{m,k}+\sigma^2_k) \geq \lambda^{\mathsf{B,t}}_{n,k}+\mu^{\mathsf{B,t}}_k,$$

$$\sum_{\forall m}(\eta^{\mathsf{S,t}}_m+\sum_{\forall k'}\beta^t_{m,k'})P^{\mathsf{S}}_m g^t_{m,k}+\sigma^2_k \leq e^{\mu^{\mathsf{B,t},(\mathrm{i})}_k}(\mu^{\mathsf{B,t}}_k-\mu^{\mathsf{B,t},(\mathrm{i})}_k+1),$$

$$\log(\beta^t_{m,k}P^{\mathsf{S}}_m g^t_{m,k}+\sum_{\forall n}(\eta^{\mathsf{B,t}}_n+\sum_{\forall k'}\alpha^t_{n,k'})P^{\mathsf{B}}_n h^t_{n,k}+\sigma^2_k)\geq\lambda^{\mathsf{S,t}}_{m,k}+\mu^{\mathsf{S,t}}_k,$$

$$\sum_{\forall n}(\eta^{\mathsf{B,t}}_n+\sum_{\forall k'}\alpha^t_{n,k'})P^{\mathsf{B}}_n h^t_{n,k}+\sigma^2_k \leq e^{\mu^{\mathsf{S,t},(\mathrm{i})}_k}(\mu^{\mathsf{S,t}}_k-\mu^{\mathsf{S,t},(\mathrm{i})}_k+1). \quad (14)$$

Proof: Consider function $f(x,y) = \log(1+\frac{x}{y+c})$, $x, y \geq 0, c > 0$, constraint $f(x,y) \geq u$ is rewritten as

$$\begin{cases} \log(x+y+c) \geq u+z, & (15a) \\ \log(y+c) \leq z, & (15b) \end{cases}$$

where z is a slack variable. Taking the exponent operator to both sides of (15b) and applying first-order approximation to the exponential term yield the following convex constraints

$$\begin{cases} \log(x+y+c) \geq u+z, & (16a) \\ y+c \leq e^{z^{(i)}}(z-z^{(i)}+1), & (16b) \end{cases}$$

wherein $z^{(i)}$ is a feasible z value at iteration i. By setting $x = \alpha^t_{n,k}P^{\mathsf{B}}_n h^t_{n,k}$, $y = \sum_{\forall(m,k')}\beta^t_{m,k'}P^{\mathsf{S}}_m g^t_{m,k}$, $c = \sum_{\forall m}\eta^{\mathsf{S,t}}_m P^{\mathsf{S}}_m g^t_{m,k} + \sigma^2_k$, and $u = \lambda^{\mathsf{B,t}}_{n,k}$, we obtain two first convex constraints in (14). Subsequently, by setting $x = \beta^t_{m,k}P^{\mathsf{S}}_m g^t_{m,k}$, $y = \sum_{\forall(n,k')}\alpha^t_{n,k'}P^{\mathsf{B}}_n h^t_{n,k}$, $c = \sum_{\forall n}\eta^{\mathsf{B,t}}_n P^{\mathsf{B}}_n h^t_{n,k} + \sigma^2_k$, and $u = \lambda^{\mathsf{S,t}}_{m,k}$, we obtain two last convex constraints in (14). ∎

Thanks to Proposition 1, we obtain the successive convex problem at iteration i around feasible point $(\boldsymbol{\mu}^{\mathsf{B},(i)}, \boldsymbol{\mu}^{\mathsf{S},(i)})$ as

$$\max_{\substack{\boldsymbol{\alpha},\boldsymbol{\beta},\boldsymbol{\lambda}^{\mathsf{B}},\\ \boldsymbol{\lambda}^{\mathsf{S}},\boldsymbol{\mu}^{\mathsf{B}},\boldsymbol{\mu}^{\mathsf{S}}}} \sum_{k,t}(\sum_{\forall n}\lambda^{\mathsf{B,t}}_{n,k}+\sum_{\forall m}\lambda^{\mathsf{S,t}}_{m,k}) \text{ s.t. } (C1)\text{–}(C6), (14). \quad (17)$$

By iterative solving problem (17), we can obtain the solution for (12). However, the obtained $\boldsymbol{\alpha}$ and $\boldsymbol{\beta}$ by solving (17) are continuous. Their binary solution can be recovered as [26]

$$\text{if } \alpha^t_{n,k} \geq 1/2, \alpha^t_{n,k} = 1, \text{ else } \alpha^t_{n,k} = 0, \quad (18a)$$

$$\text{if } \beta^t_{m,k} \geq 1/2, \beta^t_{m,k} = 1, \text{ else } \beta^t_{m,k} = 0, \quad (18b)$$

The proposed algorithm is summarized in Algorithm 1.

IV. SIMULATION AND IMPLEMENTATION

This section conducts the simulation of the considered ISTNs in an urban area. First, we carry out the simulation to obtain the channel gain of UEs over time and the link budget in terms of carrier-to-interference-plus-noise-ratio (CINR) for the entire examined area. Especially, to reflect the complexity of the urban area, the ray-tracing method and actual 3D map are employed to compute the multi-path components in (1). Subsequently, based on the obtained channel gain, the numerical results for the SR problem are provided. The simulation is conducted in an area in London City. The map is divided into multiple map segments with size of $(0.005^\circ \times 0.005^\circ)$ in latitude and longitude, respectively, and the receiver grid with size of (100×100) in each map segment is considered for CINR assessment in the entire map. Additionally, one BS is deployed in each map segment at the highest building. The UE routes are obtained from the Google Navigator application. The key simulation parameters are summarized in Table. I.

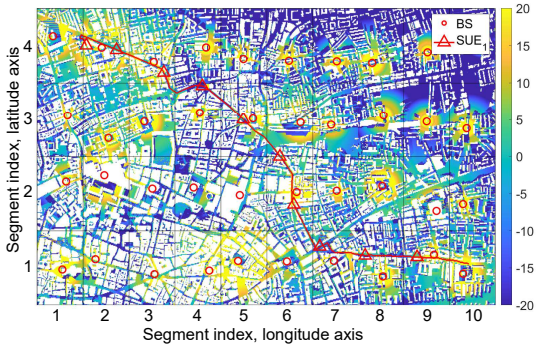

(a) Snapshot CINR heatmap of BS-UE link and UE trajectory.

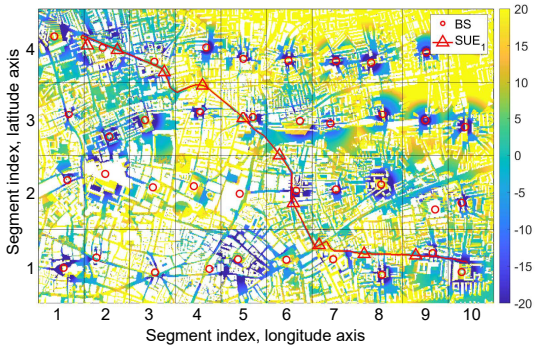

(b) Snapshot CINR heatmap of LEOSat-UE link and UE trajectory.

Fig. 2: Heatmap of CINR in dB scale with a UE trajectory.

TABLE I: Simulation Parameters

Parameter	Value
Operation frequency, f_c	3.4 GHz
System bandwidth, B	20 MHz
Latitude limitation of area	$[51.5115°\text{N}, 51.5315°\text{N}]$
Longitude limitation of area	$[0.1022°\text{W}, 0.0522°\text{W}]$
Size of one map segment	$0.005° \times 0.005°$
LEO altitude	500 km
LEO inclination angle	53°
Number of LEOSats at each time	2
LEOSat antenna parameters	[25]
Maximum transmit power of LEOSat, $P^{\mathsf{S,max}}_m$	16 dBW
Receiver point grid size in one segment	100×100 points
Maximum transmit power of BS, $P^{\mathsf{B,max}}_n$	42 dBm
Number of UEs, K	4
UE patch antenna array size	2×2
Maximum UE antenna gain	12 dBi
UE receiver noise figure, G_f	1.2 dB
UE antenna temperature, T_a	150 K
Maximum number served users at BSs, ψ^{B}_n	20
Maximum number served users at LEOSats, ψ^{S}_m	80

A. Simulation Results for Link Budget Assessment

Based on the outcome of the ray-tracing simulation, we can calculate the equivalent PL in (1). Based on the PL, the CINR is computed simply as in [27]. Subsequently, the CINR heatmaps

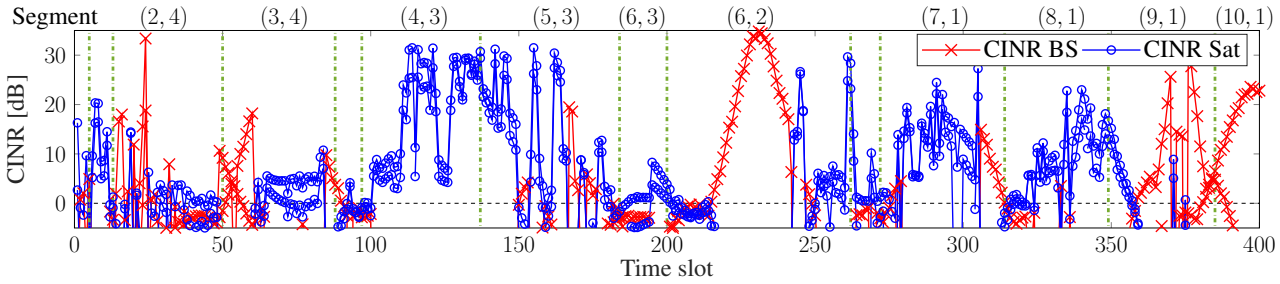

Fig. 3: CINR of links from LEOSats and BSs to a UE over TSs.

of BS-UE and LEOSat-UE links at a TS across the entire map are shown as in Fig. 2a and 2b, respectively. In addition, the trajectory of a UE is also depicted in these figures.

Regarding the BS-UE CINR in Fig. 2a, the CINR varies across the locations on the map. In particular, the BS-UE CINR at locations far from BSs and with low building density is very low, about from -10 dB to -20 dB, while that at locations near to BSs and with high building density is very high, exceeding 15 dB. This phenomenon is due to the impact of UE antenna directivity and blocking signals by buildings. Particularly, the increase in distance between BS-UE leads to the lower elevation at UE toward BSs, hence, the antenna gain decreases as per the patch antenna pattern. Additionally, at the location with lower building density, the LEOSat-UE link is less blocked, which results in a decrease in the BS-UE CINR. Besides, the LEOSat-UE CINR has the opposite trend with that of BS-UE CINR as in Fig. 2b. The LEOSat-UE CINR increases as BS-UE distance increases and the building is more sparse. This trend is also due to the influence of the UE antenna pattern and the blockage of buildings.

In addition, the UE usually moves across different segments on the map, as the depicted example UE route in Fig. 2. As a result, the CINR values change corresponding to the UE location. For an insight into the time-varying CINR as UE moving, Fig. 3 shows the BS-UE and LEOSat-UE CINR metrics over time corresponding to the UE route in Fig. 2. Compare between the CINR overtime in Fig. 3 and the CINR heatmaps in Fig. 2, it can be seen the significant changes in CINR due to the influence of the environment, especially the buildings across the locations on the map.

B. Numerical Results for Max-SR Problem

For comparison purposes, we further proposed a simple **greedy algorithm** as in Algorithm 2. For convenience, the MATLAB notation is used for the index of matrices.

Fig. 4 depicts the SR convergence of Algorithm 1 in different cases of maximum LEOSat transmit power. It can be seen that the SR increases quickly and reaches the saturation value after only about 20 iterations. In particular, at $P^{\mathsf{S},\max} = 14, 16, 18$ and 20 dBW, Algorithm 1 requires about $16, 16, 17$ and 19 iterations for convergence, respectively.

Fig. 5 depicts the SR versus the maximum transmit power at BSs of two algorithms. Interestingly, the SR provided by both algorithms has the same trend, it decreases and then increases

Algorithm 2 GREEDY ALGORITHM

Input: Parameters $\{\psi_n^{\mathsf{B}}, \psi_m^{\mathsf{S}}, \eta_n^{\mathsf{B},t}, \eta_m^{\mathsf{S},t}\}_{\forall(n,m,t)}$ and channel gain matrices $\mathbf{h} = [h_{m,k}^t]_{\forall(m,k,t)}$ and $\mathbf{g} = [g_{m,k}^t]_{\forall(n,k,t)}$
Initialize: Zero matrices $\boldsymbol{\alpha}$ and $\boldsymbol{\beta}$
for Each TS t **do**
  repeat
    Find the index of the maximum element in $\mathbf{h}(:,:,t)$: $(\hat{n}, \hat{k})$
    if $\sum_{\forall k} \alpha_{\hat{n},k}^t \leq \psi_{\hat{n}}^{\mathsf{B}} - \eta_{\hat{n}}^{\mathsf{B},t}$ **then** Update $\alpha_{\hat{n},\hat{k}}^t = 1$ and $\mathbf{h}(:,\hat{k},t) = \mathbf{0}$
    else Update $\mathbf{h}(\hat{n},:,t) := \mathbf{0}$
  until All BSs or UEs are assigned
  repeat
    Find the index of the maximum element in $\mathbf{g}(:,:,t)$: $(\hat{m}, \hat{k})$
    if $\sum_{\forall k} \beta_{\hat{m},k}^t \leq \psi_{\hat{m}}^{\mathsf{S}} - \eta_{\hat{m}}^{\mathsf{S},t}$ **then** Update $\beta_{\hat{m},\hat{k}}^t = 1$ and $\mathbf{g}(:,\hat{k},t) = \mathbf{0}$
    else Update $\mathbf{g}(\hat{m},:,t) := \mathbf{0}$
  until All LEOSats or UEs are assigned
end for
Output: Link selection solution $\boldsymbol{\alpha}, \boldsymbol{\beta}$

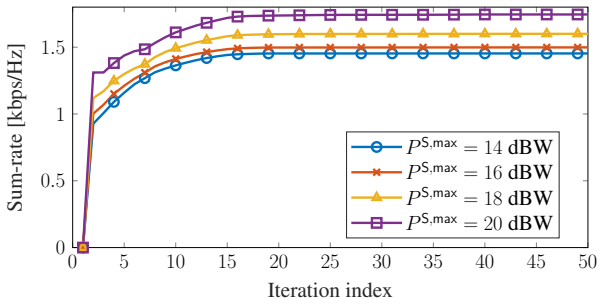

Fig. 4: The convergence rate of sum-rate over iterations.

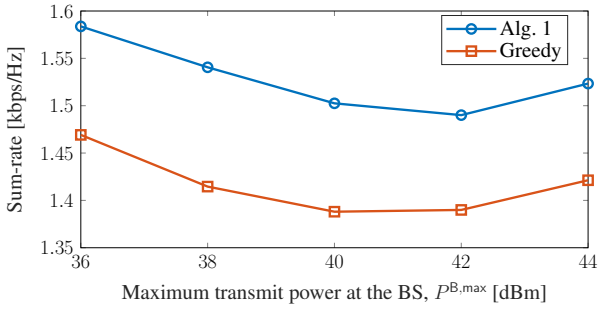

Fig. 5: Sum-rate versus the maximum transmit power at the BS.

as $P^{\mathsf{B},\max}$ increases. This phenomenon can be explained as follows. Increasing the transmit power at the BS causes cross-system interference to the signal sent from LEOSats to UEs, leading to the degradation in SR. However, exceeding a certain transmit power value, the throughput offered by BSs dominates that of the LEOSat-UE links, resulting in an increase in SR. Compared between the two algorithms, in all considered values

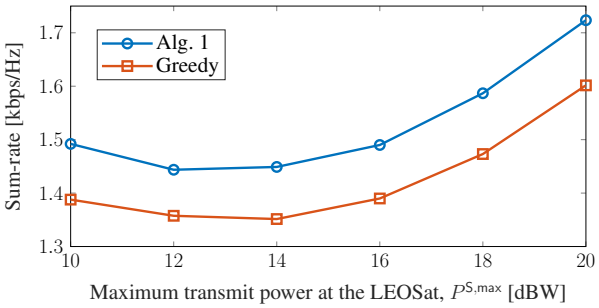

Fig. 6: Sum-rate versus the maximum transmit power at the LEOSat.

of $P^{\mathsf{B},\max}$, Algorithm 1 always provides better SR performance than that of the greedy algorithm. The performance gap between two lines is significant, about 0.11 and 0.1 kbps/Hz at $P^{\mathsf{B},\max} = 36$ dBm and $P^{\mathsf{B},\max} = 42$ dBm, respectively.

Fig. 6 illustrates the SR performance at different LEOSat power budgets. The SR evolution trend and the explanation are similar to those in Fig. 5. In addition, at $P^{\mathsf{S},\max}$ larger than 14 dBW, the throughput offered by LEOSats seems to dominate that of BS-UE links clearly since the SR increases quickly as $P^{\mathsf{S},\max}$ increases in this range. In particular, Algorithm 1 provides the SR of about 1.45 kbps/Hz and 1.73 kbps/Hz at $P^{\mathsf{S},\max} = 14$ dBW and $P^{\mathsf{S},\max} = 20$ dBW, respectively. Furthermore, Algorithm 1 outperforms the greedy algorithm in all considered cases, the gap between the two lines is about 0.1 kbps/Hz. These numerical results have demonstrated the efficiency of Algorithm 1 compared to the greedy algorithm.

V. Conclusion

This work studied the time-window ISTNs in realistic urban environments wherein cross-system interference is considered. The system is highly dynamic due to the UE and LEOSat movements. Hence, We formulated an SR maximization problem to optimize UE link selection over time. To address this efficiently, we employed the SCA method to develop an iterative algorithm. In the simulation, to capture the effect of urban area characteristics on the channels from LEOSats and BSs to UEs, the ray-tracing method and realistic 3D map are utilized. The resulting CINR heatmap offered valuable insights into the impact of urban environments on ISTNs. Numerical results demonstrated that our proposed algorithm outperformed the greedy algorithm in terms of SR performance.

Acknowledgment

This work has been supported by the Luxembourg National Research Fund (FNR) under the project INSTRUCT (IPBG19/14016225/INSTRUCT) and project MegaLEO (C20/IS/14767486).

References

[1] C.-X. Wang *et al.*, "On the road to 6G: Visions, requirements, key technologies, and testbeds," *IEEE Commun. Surveys Tut.*, vol. 25, no. 2, pp. 905–974, Secondquarter 2023.

[2] H. Tataria *et al.*, "6G wireless systems: Vision, requirements, challenges, insights, and opportunities," *Proceedings of the IEEE*, vol. 109, no. 7, pp. 1166–1199, July 2021.

[3] Z. Abdullah *et al.*, "Integrated access and backhaul via satellites," in *IEEE PIMRC*, 2023, pp. 1–6.

[4] G. Fontanesi *et al.*, "Artificial intelligence for satellite communication and non-terrestrial networks: A survey," 2023.

[5] H. Nguyen-Kha, V. N. Ha, E. Lagunas, S. Chatzinotas, and J. Grotz, "LEO-to-user assignment and resource allocation for uplink transmit power minimization," in *Proc. WSA & SCC 2023*, 2023.

[6] ——, "Two-tier user association and resource allocation design for integrated satellite-terrestrial networks," in *IEEE ICC Workshop*, 2023.

[7] ——, "Joint two-tier user association and resource management for integrated satellite-terrestrial networks," *IEEE Trans. Wireless Commun. (to appear)*, 2024.

[8] 3GPP, "Solutions for NR to support non-terrestrial networks (NTN): Non-terrestrial networks (NTN) related RF and co-existence aspects," 3GPP, TS 38.863, Dec. 2023, 18.0.0.

[9] FCC, "C-Band spectrum will be available for 5G services on accelerated basis," 2020.

[10] RSPG, "Opinion on 5G developments and possible implications for 6G spectrum needs and guidance on the rollout of future wireless broadband networks," 2023.

[11] H. Nguyen-Kha, V. N. Ha, E. Lagunas, S. Chatzinotas, and J. Grotz, "An experimental study of C-band channel model in integrated LEO satellite and terrestrial systems," in *Proc. MeditCom 2024*, 2024.

[12] V. N. Ha, E. Lagunas, T. S. Abdu, H. Chaker, S. Chatzinotas, and J. Grotz, "Large-scale beam placement and resource allocation design for MEO-constellation SATCOM," in *ICC Workshop - 6GSatComNet*, 2023.

[13] T. M. Kebedew, V. N. Ha, E. Lagunas, J. Grotz, and S. Chatzinotas, "Qoe-aware cost-minimizing capacity renting for satellite-as-a-service enabled multiple-beam satcom systems," *IEEE Trans. Commun.*, vol. 72, no. 3, pp. 1773–1789, 2024.

[14] J. C. M. Duncan *et al.*, "Harnessing the power of swarm satellite networks with wideband distributed beamforming," in *IEEE PIMRC*, 2023, pp. 1–6.

[15] V. N. Ha *et al.*, "User-centric beam selection and precoding design for coordinated multiple-satellite systems," in *IEEE PIMRC*, 2024.

[16] Y. Cho, H.-K. Kim, M. Nekovee, and H.-S. Jo, "Coexistence of 5g with satellite services in the millimeter-wave band," *IEEE Access*, 2020.

[17] E. Lagunas, C. G. Tsinos, S. K. Sharma, and S. Chatzinotas, "5G cellular and fixed satellite service spectrum coexistence in C-band," *IEEE Access*, vol. 8, pp. 72 078–72 094, 2020.

[18] L. Sormunen, H. Martikainen, J. Puttonen, and D. Panaitopol, "Co-existence of terrestrial and non-terrestrial networks on adjacent frequency bands," in *2022 ASMS/SPSC*, 2022, pp. 1–6.

[19] N. Okati, A. N. Barreto, L. U. Garcia, and J. Wigard, "Co-existence of terrestrial and non-terrestrial networks in S-band," arXiv, 2024.

[20] K.-H. Nguyen, H. V. Nguyen, M. T. P. Le, L. Sanguinetti, and O.-S. Shin, "On the energy efficiency maximization of NOMA-aided downlink networks with dynamic user pairing," *IEEE Access*, vol. 10, pp. 35 131–35 145, 2022.

[21] H. Nguyen-Kha, H. V. Nguyen, M. T. P. Le, and O.-S. Shin, "Optimization of UAV-mounted intelligent reflecting surface for the downlink of cellular systems," in *2022 IEEE Ninth International Conference on Communications and Electronics (ICCE)*, 2022, pp. 101–106.

[22] L. Chen, V. N. Ha, E. Lagunas, L. Wu, S. Chatzinotas, and B. Ottersten, "The next generation of beam hopping satellite systems: Dynamic beam illumination with selective precoding," *IEEE Trans. Wireless Commun.*, vol. 22, no. 4, pp. 2666–2682, 2023.

[23] H. Nguyen-Kha, H. V. Nguyen, M. T. P. Le, and O.-S. Shin, "Joint UAV placement and IRS phase shift optimization in downlink networks," *IEEE Access*, vol. 10, pp. 111 221–111 231, 2022.

[24] 3GPP, "Study on channel model for frequencies from 0.5 to 100 GHz ," 3rd Generation Partnership Project (3GPP), Technical report (TR) 38.901, Dec. 2019, 16.0.1.

[25] ——, "Study on New Radio (NR) to support non-terrestrial networks," 3rd Generation Partnership Project (3GPP), Technical report (TR) 38.811, Sept. 2020, version 15.4.0.

[26] V. N. Ha, L. B. Le, and N.-D. Dao, "Coordinated multipoint transmission design for cloud-RANs with limited fronthaul capacity constraints," *IEEE Trans. Veh. Technol.*, vol. 65, no. 9, pp. 7432–7447, 2016.

[27] A. Guidotti, A. Vanelli-Coralli, A. Mengali, and S. Cioni, "Non-terrestrial networks: Link budget analysis," in *IEEE ICC*, 2020, pp. 1–7.